

## ARTICLE TYPE

# Primordial non-Gaussianity systematics from redshift mismatch with SPHEREx

Chandra Shekhar Saraf and David Parkinson

Korea Astronomy and Space Science Institute, 776 Daedeok-daero, Yuseong-gu, Daejeon 34055, South Korea

Author for correspondence: Chandra Shekhar Saraf, Email: cssaraf@kasi.re.kr.

## Abstract

The ability to differentiate between different models of inflation through the imprint of primordial non-Gaussianity (PNG) requires a tight constraint on the local PNG parameter  $f_{\text{NL}}^{\text{loc}}$ . Future large scale structure surveys like *Euclid*, Vera C. Rubin Observatory, and the Spectro-Photometer for the History of the Universe, Epoch of Reionization, and Ices Explorer (SPHEREx) will play a crucial role in advancing our understanding of the inflationary epoch. In this light, we present forecasts on PNG with tomographic angular power spectrum from simulations of SPHEREx. We put forward the effects of redshift bin mismatch of galaxies as a source of systematic error when estimating  $f_{\text{NL}}^{\text{loc}}$  and galaxy linear halo bias. We simulate 500 SPHEREx-like galaxy density fields, and divide the galaxies into 13 redshift bins assuming Gaussian photometric redshift errors. We show that the misclassification of galaxies in redshift bins can result in strong apparent tensions on  $f_{\text{NL}}^{\text{loc}}$  up to  $\sim 3\sigma$  and up to  $\sim 9\sigma$  on galaxy bias. We propose a scattering matrix formalism to mitigate bin mismatch of galaxies and to obtain unbiased estimates of cosmological parameters from tomographic angular clustering measurements.

**Keywords:** cosmic inflation, large scale structure of the universe, cosmological models, maximum likelihood estimation

## 1. Introduction

Inflation is a widely accepted solution to the horizon and flatness problems, and provides a mechanism for the origin of the density perturbations required for the large scale structure (LSS) formation in the Universe (Starobinsky, 1980; Sato, 1981; Guth, 1981; Linde, 1982, 1983). The exact dynamics of the inflationary epoch, though, still remain a mystery at large. The current observations can be fit with a large number of models for inflation, with different predictions for the inflaton field. Earlier analyses of cosmic microwave background (CMB) and LSS pointed toward a spectrum of nearly Gaussian and scale-invariant primordial fluctuations (Komatsu et al., 2003; Tegmark et al., 2004). However, many alternative models predict non-Gaussian behaviour of the primordial fluctuations. Primordial non-Gaussianity (PNG) describes deviation from the Gaussian initial density field present after inflation. Most inflationary models suggest that non-Gaussianity depends on the local gravitational potential, and is parameterised by the  $f_{\text{NL}}^{\text{loc}}$  parameter:

$$\Phi(\mathbf{x}) = \phi(\mathbf{x}) + f_{\text{NL}}^{\text{loc}}[\phi^2(\mathbf{x}) - \langle \phi \rangle^2] + \mathcal{O}(\phi^3), \quad (1)$$

where  $\Phi$  is the primordial gravitational potential and  $\phi$  is a Gaussian random field (Komatsu & Spergel, 2001).

In general, single field slow roll inflation models predict  $|f_{\text{NL}}^{\text{loc}}| \ll 1$  (Maldacena, 2003; Creminelli & Zaldarriaga, 2004), whereas multi-field inflationary models can result in stronger non-Gaussianity with  $|f_{\text{NL}}^{\text{loc}}| \geq 1$  (Lyth et al., 2003; Zaldarriaga, 2004; Bartolo et al., 2004). Thus, to differentiate between single and multi-field inflationary models, a tight constraint on  $f_{\text{NL}}^{\text{loc}}$  with at least  $\sigma(f_{\text{NL}}^{\text{loc}}) \sim 1$  is required.

The current best constraint on  $f_{\text{NL}}^{\text{loc}}$  comes from *Planck* bispectrum measurements,  $f_{\text{NL}}^{\text{loc}} = -0.9 \pm 5.1$  (Planck Collaboration et al., 2020a). Next generation cosmic microwave background (CMB) experiments like CMB-S4 are only expected to improve the *Planck* constraints by a factor of  $\sim 2$  (Abazajian et al., 2016). In parallel, tracers of large scale structure (LSS) can be used to constraint PNG in the three-dimensional matter distribution. The current most robust LSS constraints on  $f_{\text{NL}}^{\text{loc}}$  come from eBOSS quasars with  $\sigma(f_{\text{NL}}^{\text{loc}}) = 21$  (Mueller et al., 2022), or from BOSS LRGs with  $\sigma(f_{\text{NL}}^{\text{loc}}) = 28$  (Cabass et al., 2022) and  $\sigma(f_{\text{NL}}^{\text{loc}}) = 31$  (D’Amico et al., 2022). Similar precision on  $f_{\text{NL}}^{\text{loc}}$  have also been obtained with photometric galaxy surveys (Giannantonio et al., 2014; Rezaie et al., 2024). However, systematic errors have been a challenge when estimating  $f_{\text{NL}}^{\text{loc}}$  with photometric surveys (Pullen & Hirata, 2013; Leistedt & Peiris, 2014) or even with spectroscopic surveys (Rezaie et al., 2021).

The constraints on  $f_{\text{NL}}^{\text{loc}}$  can be significantly improved by combining information from different LSS tracers (Fonseca et al., 2017, 2018; Schmittfull & Seljak, 2018; Jolicoeur et al., 2023; Sullivan et al., 2023). One of the avenues to reduce systematic errors is to perform tomographic cross-correlations with surveys like Dark Energy Spectroscopic Instrument (DESI; DESI Collaboration et al. 2016), *Euclid* (Euclid Collaboration et al., 2024), Vera C. Rubin Observatory Legacy Survey of Space and Time (LSST; LSST Science Collaboration et al. 2009; Ivezić et al. 2019), and Spectro-Photometer for the History of the Universe, Epoch of Reionization, and Ices Explorer (SPHEREx; Doré et al. 2014). However, tomographic correlations are inherently plagued by misclassified galaxies in redshift

bins due to photometric redshift errors (hereafter, photo- $z$  errors). We identified the impact and mitigation strategy for this redshift bin mismatch of galaxies with simulations of LSST survey in Shekhar Saraf & Bielewicz (2024) (hereafter, C24). The main goal of this paper is to forecast the effects of redshift bin mismatch when estimating  $f_{\text{NL}}^{\text{loc}}$  from tomographic galaxy angular power spectra with SPHEREx.

SPHEREx<sup>a</sup> is a NASA medium class space-based observatory that will conduct the first near-infrared spectro-photometric all-sky survey in the wavelength range  $0.75 < \lambda < 5.0 \mu\text{m}$ . During its nominal 25 months mission, SPHEREx will measure the large scale three-dimensional distribution of galaxies. Redshifts for these galaxies will be photometrically determined by fitting templates to spectra, leveraging the nearly-universal  $1.6 \mu\text{m}$  bump. With launch scheduled for February 2025, SPHEREx will be the next major experiment to test the theories of inflation. This paper is, then, a timely addition to address the PNG systematics from redshift bin mismatch with SPHEREx.

The paper is arranged as follows: Section 2 outlines the theoretical background for modelling the angular power spectrum, Section 3 describes the simulation setup, methodology for propagation of photo- $z$  errors and estimation of  $f_{\text{NL}}^{\text{loc}}$  from power spectra. Our results are presented in Section 4 and Section 5 summarizes our findings and future prospects.

## 2. Theory

Local PNG will increase the amplitude of the halo power spectrum on large scales, resulting in a scale dependent halo bias given by (Slosar *et al.*, 2008; Dalal *et al.*, 2008)

$$b_h(k, z) = b_L(z) + f_{\text{NL}}^{\text{loc}} [b_L(z) - 1] \delta_c \frac{3\Omega_m H_0^2}{k^2 T(k) D(z)} \quad (2)$$

where  $b_L(z)$  is the linear halo bias and  $\delta_c (= 1.686)$  is the critical over-density for spherical collapse at  $z = 0$ .  $\Omega_m$  and  $H_0$  are the matter density parameter and Hubble parameter at  $z = 0$ ,  $T(k)$  is the linear matter transfer function normalised to 1 at low  $k$ , and  $D(z)$  is the growth factor. The  $f_{\text{NL}}^{\text{loc}}$  parameter can be measured directly from galaxy angular power spectrum or bispectrum when spectroscopic redshifts are available (Ross *et al.*, 2013; Gomes *et al.*, 2020; Moradinezhad Dizgah *et al.*, 2021). However, when spectroscopic data is not available, the galaxy bispectrum cannot be computed reliably. In this case, a tomographic analysis with galaxy auto-power spectra can be used to estimate  $f_{\text{NL}}^{\text{loc}}$ .

For tomographic analysis, the galaxy angular power spectrum between bins  $i$  and  $j$  is given by

$$C_\ell^{ij} = \frac{2}{\pi} \int dk k^2 W_\ell^i(k) W_\ell^j(k) P(k) \quad (3)$$

where  $P(k)$  is the matter power spectrum at redshift  $z = 0$  computed using CAMB (Lewis *et al.*, 2000).  $W_\ell^i(k)$  is the galaxy window function in the  $i$ th tomographic bin

$$W_\ell^i(k) = \int dz \frac{dN^i}{dz} D(z) b_h^i(k, z) j_\ell(k\chi(z)) \quad (4)$$

<sup>a</sup><https://spherex.caltech.edu>

where  $\frac{dN^i}{dz}$  is the redshift distribution of galaxies and  $j_\ell(k\chi)$  are spherical Bessel functions. For the range of scales included in the forecast, we used  $k_{\text{min}} = 0.001 h/\text{Mpc}$  and  $k_{\text{max}} = 0.25 h/\text{Mpc}$ . Except  $f_{\text{NL}}^{\text{loc}}$ , the rest of the cosmological parameters were assumed fixed with values quoted in Table 1.

**Table 1.** List of cosmological parameters assumed fixed in our simulations (taken from Planck Collaboration *et al.* 2020b).

$\Omega_{c,0}$	$\Omega_{b,0}$	$H_0^a$	$\sigma_8$	$n_s$
0.265	0.049	67.32	0.811	0.9645

<sup>a</sup> in  $\text{km s}^{-1} \text{Mpc}^{-1}$

## 3. Simulations and methodology

We used the publicly available code GLASS (Tessore *et al.*, 2023) to create 500 Monte Carlo simulations of lognormal galaxy density field covering 70% of the sky (excluding the galactic plane), and galaxy redshifts  $z_t$ . The photo- $z$ s for galaxies  $z_p$  were generated by drawing a positive random value from Gaussian distribution  $\mathcal{N}(z_t, \sigma_0(1+z))$ , such that the galaxy number density follows expected SPHEREx redshift accuracy shown in left panel of Fig. 1. The fiducial evolution of linear halo bias used in simulations is shown with black dashed line in the right panel of Fig. 1.

We divided each simulated galaxy catalogue into 13 disjoint redshift bins, based on their photo- $z$ s, with  $\Delta z = 0.1$  between  $0.0 < z \leq 1.3$ . We performed simulations for three different values of  $f_{\text{NL}}^{\text{loc}} = 1, 10,$  and  $100$ .

We built galaxy over-density maps from photometric number count maps at HEALPix (Górski *et al.*, 2005) resolution  $N_{\text{side}} = 256$  using

$$g(\hat{n}) = \frac{n(\hat{n}) - \bar{n}}{\bar{n}}, \quad (5)$$

where  $n(\hat{n})$  is the number of galaxies at angular position  $\hat{n}$ , and  $\bar{n}$  is the mean number of galaxies per pixel.

### 3.1 Estimating the power spectra

We used the MASTER algorithm (Hivon *et al.*, 2002) implemented in NaMASTER (Alonso *et al.*, 2019) to compute the full sky power spectra in every tomographic bin. We binned the power spectra in bins of  $\Delta\ell = 10$  from  $\ell = 2$  to  $\ell = 80$ . We computed the sample covariance matrix in each tomographic bin from 500 simulations using

$$\mathbf{K}_{\ell\ell'}^{gg,gg} = \frac{1}{N_s - 1} \sum_{i=1}^{N_s} \left( \tilde{C}_\ell^{gg,i} - \langle \tilde{C}_\ell^{gg} \rangle \right) \left( \tilde{C}_{\ell'}^{gg,i} - \langle \tilde{C}_{\ell'}^{gg} \rangle \right), \quad (6)$$

where  $N_s$  is the total number of simulations,  $\tilde{C}_\ell^{gg,i}$  is the power spectrum estimated from the  $i$ th simulation and

$$\langle \tilde{C}_\ell^{gg} \rangle = \frac{1}{N_s} \sum_{i=1}^{N_s} \tilde{C}_\ell^{gg,i} \quad (7)$$

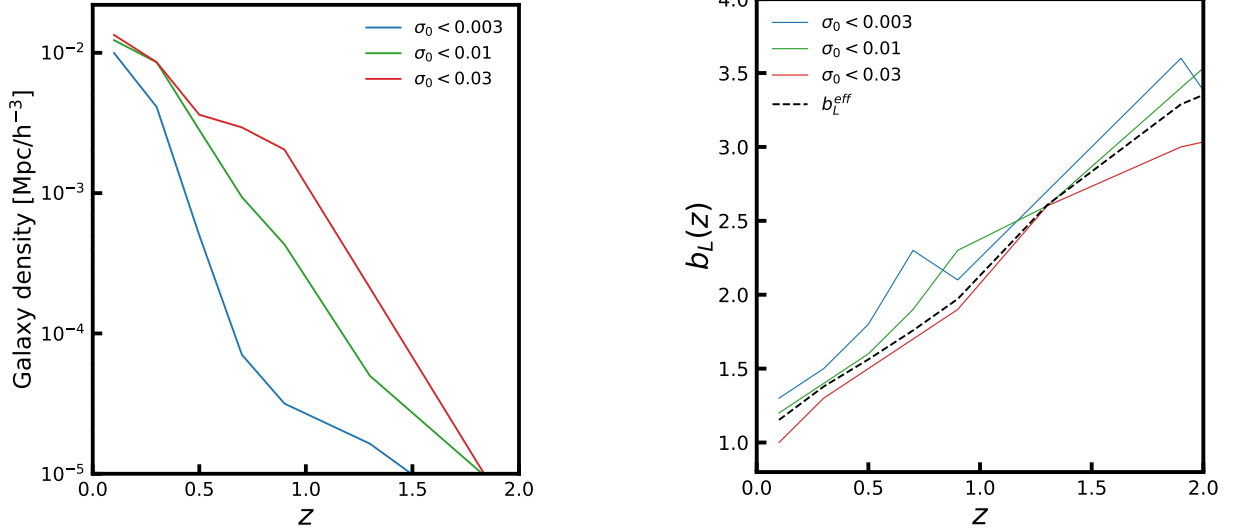


**Figure 1.** Fiducial data used in our simulations taken from Doré et al. (2014). *Left:* The comoving number density of galaxies in different redshift accuracy bins. *Right:* The galaxy linear halo bias in different redshift accuracy bins. The effective galaxy bias used in our simulations is shown with black dashed line.

### 3.2 Propagation of photo-z errors

We accounted for photo-z uncertainties in our analysis by convoluting the photometric redshift distribution with the conditional probability  $p(z_i - z_p | z_p)$ , which we call the photo-z error distribution. An estimate of the true redshift distribution for  $i$ th tomographic bin can then be given as

$$\frac{dN^i(z)}{dz} = \int dz_p \frac{dN(z_p)}{dz_p} \Theta^i(z_p) p^i(z - z_p | z_p), \quad (8)$$

where  $\frac{dN(z_p)}{dz_p}$  is the observed photometric redshift distribution of galaxies, and  $\Theta^i(z_p)$  is a step function defining the  $i$ th redshift bin,

$$\Theta^i(z) = \begin{cases} 1, & \text{if } z_{\min}^i \leq z < z_{\min}^{i+1} \\ 0, & \text{otherwise.} \end{cases} \quad (9)$$

The true galaxy redshift distributions obtained from convolution are shown in Fig. 2. The blue lines represent how the disjoint redshift bins transform due to photo-z errors. The dashed vertical orange lines mark the boundaries of the redshift bins.

### 3.3 Parameter estimation

To forecast constraints on  $f_{\text{NL}}^{\text{loc}}$  parameter we used the maximum likelihood estimation method. The log-likelihood function takes the form

$$\log \mathcal{L} = -\frac{1}{2} [\mathbf{d}_\ell - \mathbf{t}_\ell(\theta)]^\top (\mathbf{K}_{\ell\ell'})^{-1} [\mathbf{d}_\ell - \mathbf{t}_\ell(\theta)], \quad (10)$$

where  $\mathbf{d}_\ell = \{ \langle \tilde{C}_\ell^{gg} \rangle \}$  is the joint data vector from 13 redshift bins,  $\mathbf{t}_\ell(\theta)$  is the theory vector,  $\theta$  represents the free parameters

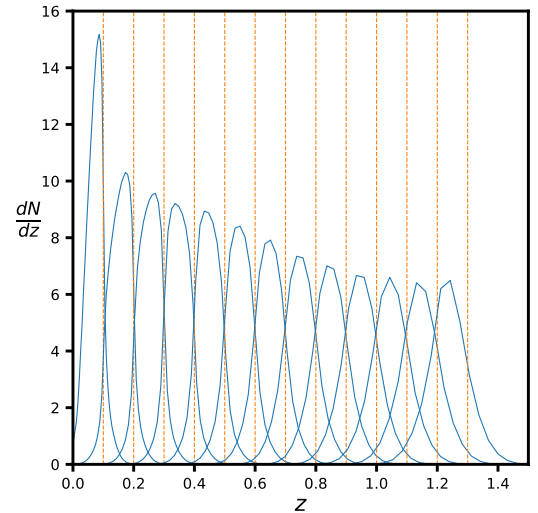


**Figure 2.** Effect of photo-z scatter on tomographic redshift distributions. The dashed orange lines mark the boundaries of redshift bins. The blue solid curves are the redshift distributions obtained after convolution.

set (13 galaxy bias parameters +  $f_{\text{NL}}^{\text{loc}}$ ), and  $\mathbf{K}_{\ell\ell'}$  is the joint covariance matrix given by

$$\mathbf{K}_{\ell\ell'} = \begin{bmatrix} \mathbf{K}_{\ell\ell'}^{g_1 g_1, g_1 g_1} & \mathbf{K}_{\ell\ell'}^{g_1 g_1, g_2 g_2} & \dots & \mathbf{K}_{\ell\ell'}^{g_1 g_1, g_{13} g_{13}} \\ \mathbf{K}_{\ell\ell'}^{g_2 g_2, g_1 g_1} & \mathbf{K}_{\ell\ell'}^{g_2 g_2, g_2 g_2} & \dots & \mathbf{K}_{\ell\ell'}^{g_2 g_2, g_{13} g_{13}} \\ \vdots & \vdots & \ddots & \vdots \\ \mathbf{K}_{\ell\ell'}^{g_{13} g_{13}, g_1 g_1} & \mathbf{K}_{\ell\ell'}^{g_{13} g_{13}, g_2 g_2} & \dots & \mathbf{K}_{\ell\ell'}^{g_{13} g_{13}, g_{13} g_{13}} \end{bmatrix}. \quad (11)$$

We used flat priors for parameters in the range  $b_L \in [0, 20]$  and  $f_{\text{NL}}^{\text{loc}} \in [-100, 200]$ . We used the EMCEE package (Foreman-Mackey et al., 2013) to effectively sample the parameter space.

## 4. Results

### 4.1 Pipeline validation without redshift errors

Before discussing the effects of photo- $z$  errors on parameters, it is worth to validate our analysis pipeline. We did this by estimating  $f_{\text{NL}}^{\text{loc}}$  and galaxy bias from simulations before adding photo- $z$  errors. The recovered values of  $f_{\text{NL}}^{\text{loc}}$  parameter are shown in Fig. 7. We note that there are no intrinsic systematics in our analysis pipeline. In the following sections, we present the effects of photo- $z$  errors on  $f_{\text{NL}}^{\text{loc}}$  and galaxy bias.

### 4.2 Constraints on $f_{\text{NL}}^{\text{loc}}$ and galaxy bias

The  $f_{\text{NL}}^{\text{loc}}$  posteriors estimated after adding photo- $z$  errors are shown in Fig. 3 with green histograms. The vertical red lines mark the fiducial values of  $f_{\text{NL}}^{\text{loc}}$  used for simulations. We found 1–3  $\sigma$  offsets in the estimated values of  $f_{\text{NL}}^{\text{loc}}$  even after accounting for photo- $z$  errors as described in Section 3.2. The constraints on galaxy bias for  $f_{\text{NL}}^{\text{loc, true}} = 1$  are shown in Fig. 4 with green circles. The dashed red line represent the evolution of galaxy bias assumed in our simulations. The galaxy bias shows deviations up to  $\sim 9\sigma$  from the fiducial evolution, and follows similar trend in simulations with  $f_{\text{NL}}^{\text{loc, true}} = 10, 100$ . The 1D and 2D posteriors of parameters for  $f_{\text{NL}}^{\text{loc, true}} = 1, 10, 100$  are shown in Fig. 8–10, respectively.

We note that we did not use the cross-power spectra between redshift bins to refine the tomographic redshift distributions in Eq. 8. However, to assess the robustness of our estimated parameters against the redshift distribution, we replaced  $\frac{dN^i(z)}{dz}$  computed through convolution (Section 3.2) with one derived directly from a simulated catalogue by tracking individual galaxies in the simulation. This substitution allows us to replace the estimated true redshift distribution with its theoretical prediction. Even with this change, we observed similar offsets in both  $f_{\text{NL}}^{\text{loc}}$  and galaxy bias parameters. This indicates that the observed differences in the parameter estimates do not stem from any biased estimates of  $\frac{dN^i(z)}{dz}$ . These differences are instead due to systematics present in the data which we refer to as “redshift bin mismatch”.

The observed offsets in parameters are due to the fact that photo- $z$  errors cause galaxies to be classified in wrong redshift bins. The diffusion of galaxies across tomographic bins result in significant differences from the underlying true power spectrum at all scales, as shown in Fig. 5. We performed a detailed study on the impact of bin mismatch with  $\sigma_8$  parameter, and its mitigation in C24. In the following section, we briefly describe the mitigation strategy for unbiased measurements of  $f_{\text{NL}}^{\text{loc}}$  parameter.

### 4.3 Correction for redshift bin mismatch

As mentioned above, the parameters estimated in a tomographic angular correlation analyses will be biased due to galaxies ending up in the wrong redshift bin owing to their photo- $z$  errors. The redshift bin mismatch couples the power

spectra computed from true redshifts  $C^{\text{gg, tr}}(\ell)$  to that from photometric redshifts  $C^{\text{gg, ph}}(\ell)$  (Zhang *et al.*, 2010):

$$C_{ij}^{\text{gg, ph}}(\ell) = \sum_{x,y} P_{xi} P_{yj} C_{xy}^{\text{gg, tr}}(\ell), \quad (12)$$

where  $i, j, x, y$  denote tomographic bins and  $P_{ij}$  represents the fraction of galaxies moving from redshift bin  $i \rightarrow j$  due to photo- $z$  errors. We can re-write Eq. 12 in the matrix form as:

$$C^{\text{gg, ph}} = P^\top C^{\text{gg, tr}} P \quad (13)$$

where  $P$  is now called the scattering matrix. We compute coefficients  $P_{ij}$  directly from the redshift distribution as the ratio

$$P_{ij} = \int_{z_{\min}^j}^{z_{\min}^{j+1}} dz \frac{dN^i}{dz} / \int_{z_{\min}^j}^{z_{\min}^{j+1}} dz_p \frac{dN}{dz_p}, \quad (14)$$

where  $\frac{dN}{dz_p}$  is the photometric redshift distribution of the galaxies, and  $z_{\min}^j$  is the lower limit of the  $j$ th redshift bin. We refer the readers to C24 for a more detailed explanation on the scattering matrix formalism. The average scattering matrix computed from 500 simulations for  $f_{\text{NL}}^{\text{loc, true}} = 1$  is shown in Fig. 6.

We show the results of parameters estimated with the scattering matrix formalism in Fig. 3 with orange histograms and Fig. 4 with orange circles. We note that the scattering matrix formalism yields unbiased estimates of  $f_{\text{NL}}^{\text{loc}}$  as well recovers the correct evolution of galaxy bias. We would like to point out that the power spectra  $C^{\text{gg, ph}}$  becomes a linear combination of  $C^{\text{gg, tr}}$  with quadratic weights  $P_{ij}$ . This mixing of power from different true redshift bins may not be accurately captured by only a precise estimate of the true redshift distribution, and so this inaccurate prediction will result in systematic offsets in the derive distribution of parameters. We, thus, propose to implement our scattering matrix approach when estimating parameters from tomographic angular clustering measurements in the future.

## 5. Summary

The differentiation between single and multi-field inflationary scenarios is hinged upon the measurements of local primordial non-Gaussianity. A tight constraint of  $\sigma(f_{\text{NL}}^{\text{loc}}) \sim 1$ , required to understand the dynamics of inflaton field, will be possible with the combinations of future CMB experiments and large-scale structure surveys. The next-generation of photometric surveys like LSST and SPHEREx will be crucial in measuring  $f_{\text{NL}}^{\text{loc}}$  by the means of the tomographic angular clustering measurements. However, as argued in Shekhar Saraf & Bielewicz (2024) and Saraf *et al.* (2024), tomographic measurements suffer from misclassification of galaxies into redshift bins due to their photometric redshift errors. In this work, we forecast constraints on  $f_{\text{NL}}^{\text{loc}}$  under the influence of redshift bin mismatch of galaxies.

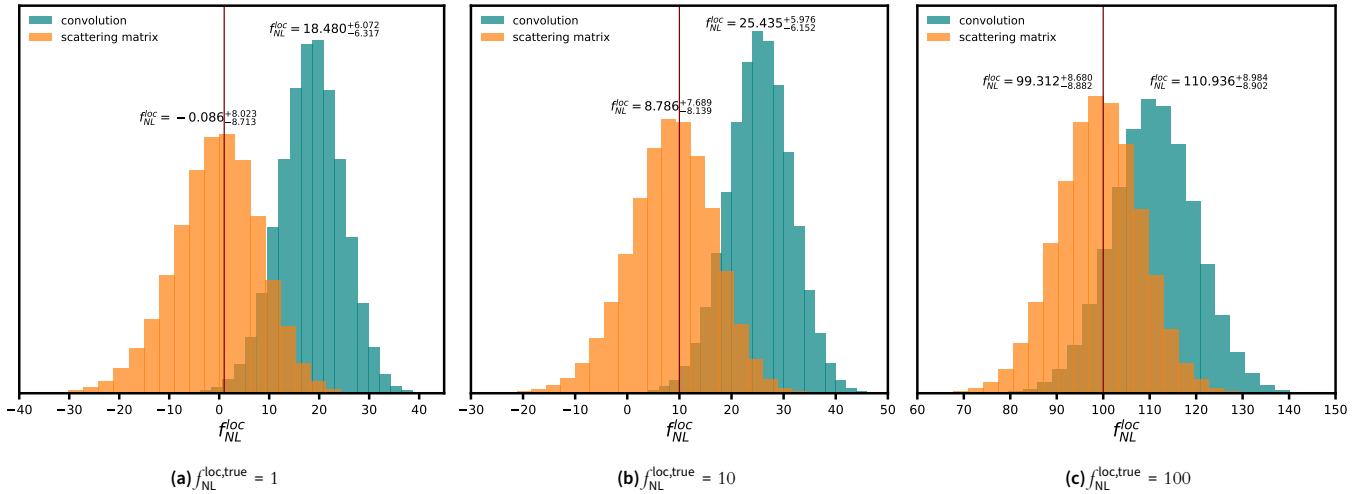


**Figure 3.** The best-fit values of  $f_{NL}^{loc}$  parameter estimated from the average power spectra of 500 realisations after adding photo- $z$  errors. The vertical red line marks the true value of  $f_{NL}^{loc}$  parameter used in simulations. The green histograms are the posteriors obtained following the convolution method to account for photo- $z$  errors. The orange histograms are the posteriors obtained from the scattering matrix approach.

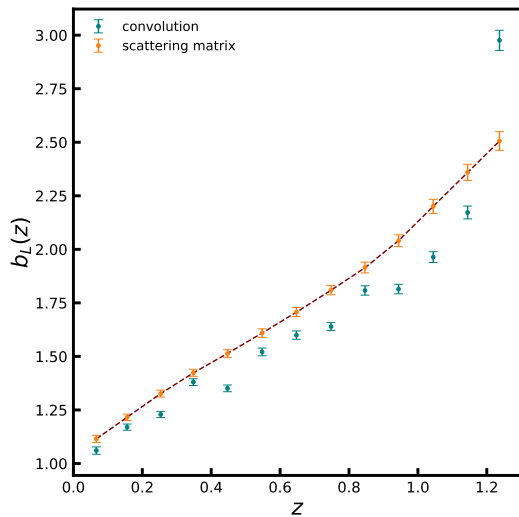


**Figure 4.** The galaxy halo bias evolution estimated from the average power spectra of 500 realisations after adding photo- $z$  errors. The dashed red line marks the fiducial evolution of  $b_L(z)$ . The green circles are best-fit values of galaxy bias obtained from the convolution method, while the orange circles are those estimated with the scattering matrix approach.

We prepared 500 log-normal galaxy density simulations using GLASS, having physical properties consistent with SPHEREx specifications. We created photometric redshifts for galaxies assuming Gaussian error distribution in three SPHEREx redshift accuracy bins (see Fig.1). We divided the galaxies into 13 redshift bins and computed the angular power spectrum in each tomographic bin. We estimated the true redshift distribution from photometric redshift distribution by the convolution method (section 3.2). The constraints on  $f_{NL}^{loc}$  were obtained from the measured angular power spectra by employing the maximum likelihood estimator.

Due to diffusion of galaxies across redshift bins, the measured galaxy angular power spectra differ significantly than the

underlying true angular power spectra (Fig. 5). This results in  $1 - 3\sigma$  offsets for  $f_{NL}^{loc}$  and up to  $\sim 9\sigma$  deviations for galaxy linear halo bias. We found similar offsets in  $f_{NL}^{loc}$  and galaxy halo bias with redshift distributions computed directly from the simulated catalogue. Finally, we showed in Section 4.3 that our scattering matrix formalism has the potential to mitigate the redshift bin mismatch of galaxies, and recover both  $f_{NL}^{loc}$  and galaxy bias within  $1\sigma$  errors.

We point out that more common approaches to estimating the true redshift distribution like convolution or deconvolution are insufficient to counter the redshift bin mismatch of galaxies. With tomographic measurements using photometric surveys, bin mismatch can lead to apparent tensions on parameters and biased inferences about cosmological models. We, therefore, propose that the scattering matrix formalism be used for future tomographic studies. This work presented the impact of photometric redshift errors on  $f_{NL}^{loc}$  measured with the angular power spectrum only. We reserve studies on the impact of other survey systematics like catastrophic redshift errors, photometric calibration errors, and joint forecasts using two and three-point angular correlation for future works.

## Acknowledgement

The authors thank Bomee Lee for stimulating discussions on constraining primordial non-Gaussianity with SPHEREx.

**Competing Interests** The author(s) declare none.

**Data Availability Statement** The simulated catalogues and analysis pipelines will be made available at reasonable requests from authors.

## References

Abazajian, K. N., Adshead, P., Ahmed, Z., et al. 2016, arXiv e-prints, arXiv:1610.02743

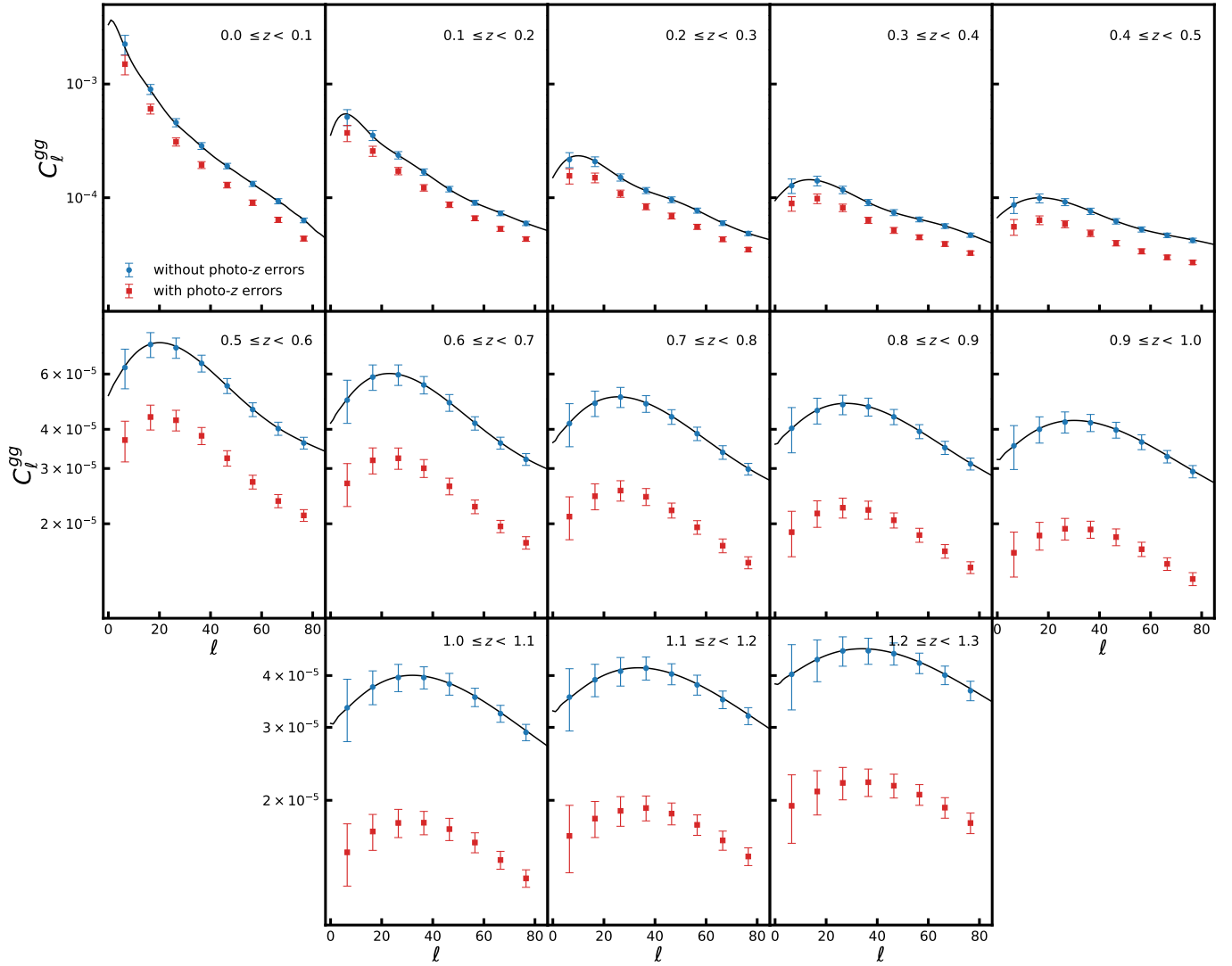


**Figure 5.** The galaxy angular power spectrum measured from 500 simulations. The black line represents the underlying true power spectrum. The blue circles are the power spectra estimated before adding photo- $z$  errors. The red squares show the power spectra after adding photo- $z$  errors. The error bars on the data points are standard errors computed from the diagonal of the sample covariance matrices (Eq. 6).

Alonso, D., Sanchez, J., Slosar, A., & LSST Dark Energy Science Collaboration. 2019, *MNRAS*, 484, 4127

Bartolo, N., Komatsu, E., Matarrese, S., & Riotto, A. 2004, *Phys. Rep.*, 402, 103

Cabass, G., Ivanov, M. M., Philcox, O. H. E., Simonović, M., & Zaldarriaga, M. 2022, *Phys. Rev. D*, 106, 043506

Creminelli, P., & Zaldarriaga, M. 2004, *J. Cosmology Astropart. Phys.*, 2004, 006

Dalal, N., Doré, O., Huterer, D., & Shirokov, A. 2008, *Phys. Rev. D*, 77, 123514

D’Amico, G., Lewandowski, M., Senatore, L., & Zhang, P. 2022, arXiv e-prints, arXiv:2201.11518

DESI Collaboration, Aghamousa, A., Aguilar, J., et al. 2016, arXiv e-prints, arXiv:1611.00036

Doré, O., Bock, J., Ashby, M., et al. 2014, arXiv e-prints, arXiv:1412.4872

Euclid Collaboration, Mellier, Y., Abdurro’uf, et al. 2024, arXiv e-prints, arXiv:2405.13491

Fonseca, J., Maartens, R., & Santos, M. G. 2017, *MNRAS*, 466, 2780

—. 2018, *MNRAS*, 479, 3490

Foreman-Mackey, D., Hogg, D. W., Lang, D., & Goodman, J. 2013, *PASP*, 125, 306

Giannantonio, T., Ross, A. J., Percival, W. J., et al. 2014, *Phys. Rev. D*, 89, 023511

Gomes, Z., Camera, S., Jarvis, M. J., Hale, C., & Fonseca, J. 2020, *MNRAS*, 492, 1513

Górski, K. M., Hivon, E., Banday, A. J., et al. 2005, *ApJ*, 622, 759

Guth, A. H. 1981, *Phys. Rev. D*, 23, 347

Hivon, E., Górski, K. M., Netterfield, C. B., et al. 2002, *ApJ*, 567, 2

Ivezić, Ž., Kahn, S. M., Tyson, J. A., et al. 2019, *ApJ*, 873, 111

Jolicoeur, S., Maartens, R., & Dlamini, S. 2023, *European Physical Journal C*, 83, 320

Komatsu, E., & Spergel, D. N. 2001, *Phys. Rev. D*, 63, 063002

Komatsu, E., Kogut, A., Nolta, M. R., et al. 2003, *ApJS*, 148, 119

Leistedt, B., & Peiris, H. V. 2014, *MNRAS*, 444, 2

Lewis, A., Challinor, A., & Lasenby, A. 2000, *ApJ*, 538, 473

Linde, A. D. 1982, *Physics Letters B*, 108, 389

—. 1983, *Physics Letters B*, 129, 177

LSST Science Collaboration, Abell, P. A., Allison, J., et al. 2009, arXiv e-prints, arXiv:0912.0201

Lyth, D. H., Ungarelli, C., & Wands, D. 2003, *Phys. Rev. D*, 67, 023503

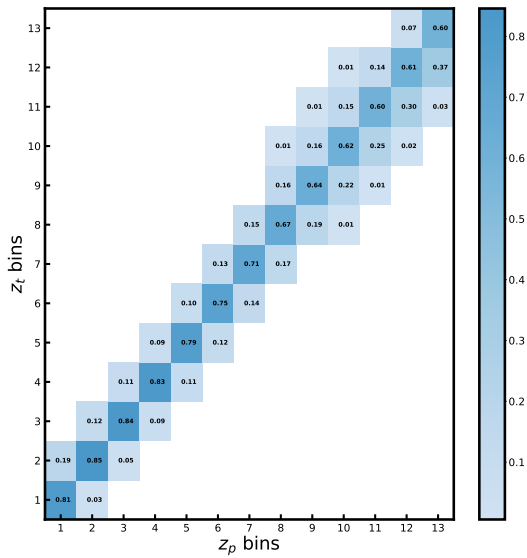


**Figure 6.** The average scattering matrix estimated from 500 simulations using Eq. 14.

- Maldacena, J. 2003, *Journal of High Energy Physics*, 2003, 013
- Moradinezhad Dizgah, A., Biagetti, M., Sefusatti, E., Desjacques, V., & Noreña, J. 2021, *J. Cosmology Astropart. Phys.*, 2021, 015
- Mueller, E.-M., Rezaie, M., Percival, W. J., et al. 2022, *MNRAS*, 514, 3396
- Planck Collaboration, Akrami, Y., Arroja, F., et al. 2020a, *A&A*, 641, A9
- Planck Collaboration, Aghanim, N., Akrami, Y., et al. 2020b, *A&A*, 641, A6
- Pullen, A. R., & Hirata, C. M. 2013, *PASP*, 125, 705
- Rezaie, M., Ross, A. J., Seo, H.-J., et al. 2021, *MNRAS*, 506, 3439
- . 2024, *MNRAS*, 532, 1902
- Ross, A. J., Percival, W. J., Carnero, A., et al. 2013, *MNRAS*, 428, 1116
- Saraf, C. S., Bielewicz, P., & Chodorowski, M. 2024, *A&A*, 690, A338
- Sato, K. 1981, *MNRAS*, 195, 467
- Schmittfull, M., & Seljak, U. 2018, *Phys. Rev. D*, 97, 123540
- Shekhar Saraf, C., & Bielewicz, P. 2024, *A&A*, 687, A150
- Slosar, A., Hirata, C., Seljak, U., Ho, S., & Padmanabhan, N. 2008, *J. Cosmology Astropart. Phys.*, 2008, 031
- Starobinsky, A. A. 1980, *Physics Letters B*, 91, 99
- Sullivan, J. M., Pijon, T., & Seljak, U. 2023, *J. Cosmology Astropart. Phys.*, 2023, 004
- Tegmark, M., Strauss, M. A., Blanton, M. R., et al. 2004, *Phys. Rev. D*, 69, 103501
- Tessore, N., Loureiro, A., Joachimi, B., von Wietersheim-Kramsta, M., & Jeffrey, N. 2023, *The Open Journal of Astrophysics*, 6, 11
- Zaldarriaga, M. 2004, *Phys. Rev. D*, 69, 043508
- Zhang, P., Pen, U.-L., & Bernstein, G. 2010, *MNRAS*, 405, 359

## Appendix 1. Pipeline validation results

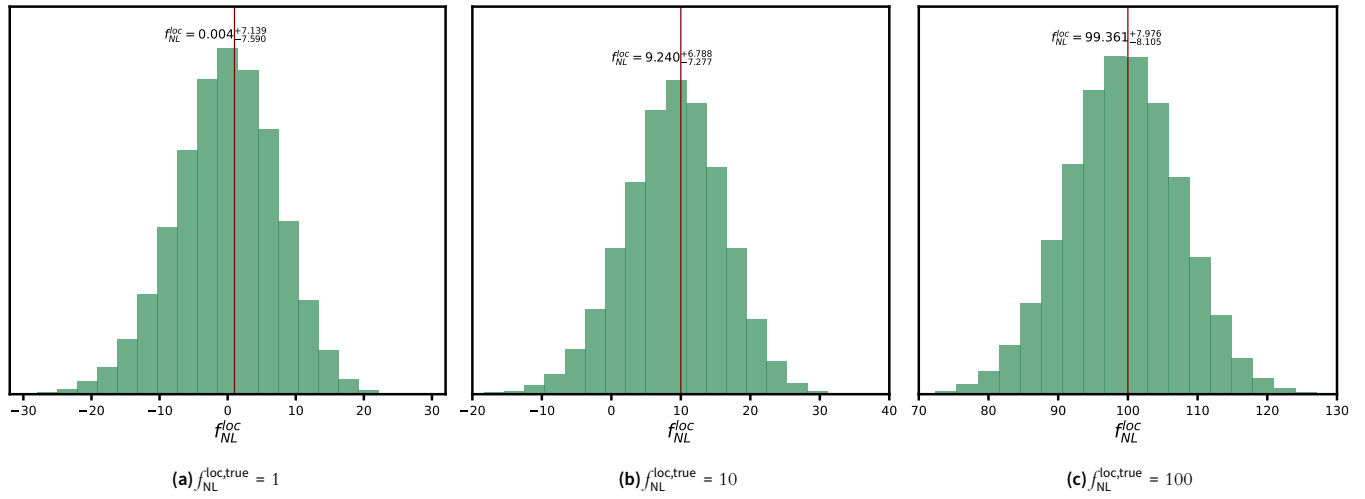


**Figure 7.** The best-fit values of  $f_{NL}^{loc}$  parameter estimated from the average power spectra of 500 realisations before adding photo- $z$  errors. The vertical red line marks the true value of  $f_{NL}^{loc}$  parameter used in simulations.

## Appendix 2. Full likelihood plots



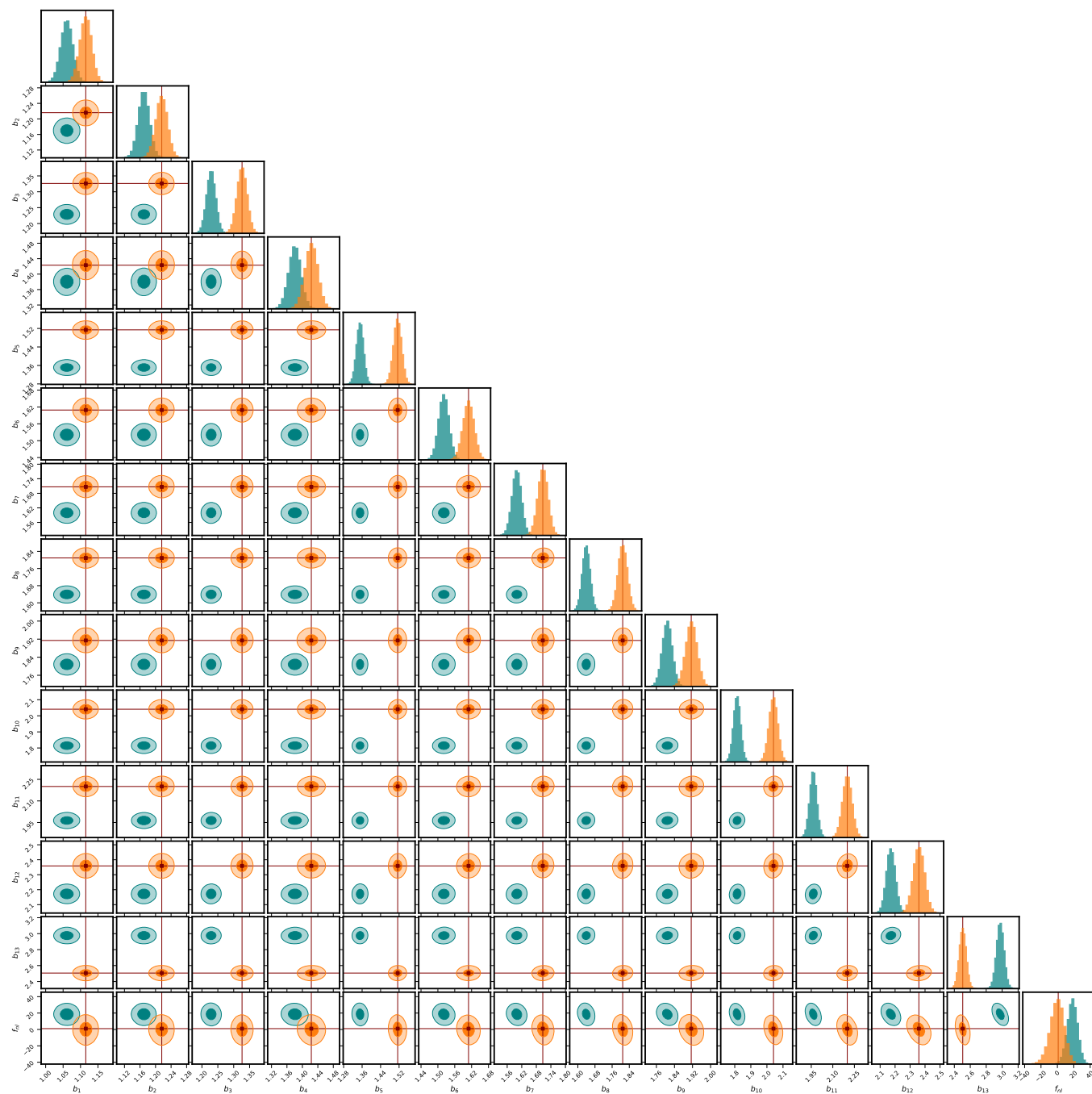


**Figure 8.** Parameter posteriors obtained from maximum likelihood estimation for  $r_{NL}^{\text{loc,true}} = 1$ . The green histograms are the posteriors obtained following the convolution method to account for photo- $z$  errors, while the orange histograms are from the scattering matrix approach. The red lines are the true values of parameters used in simulations.

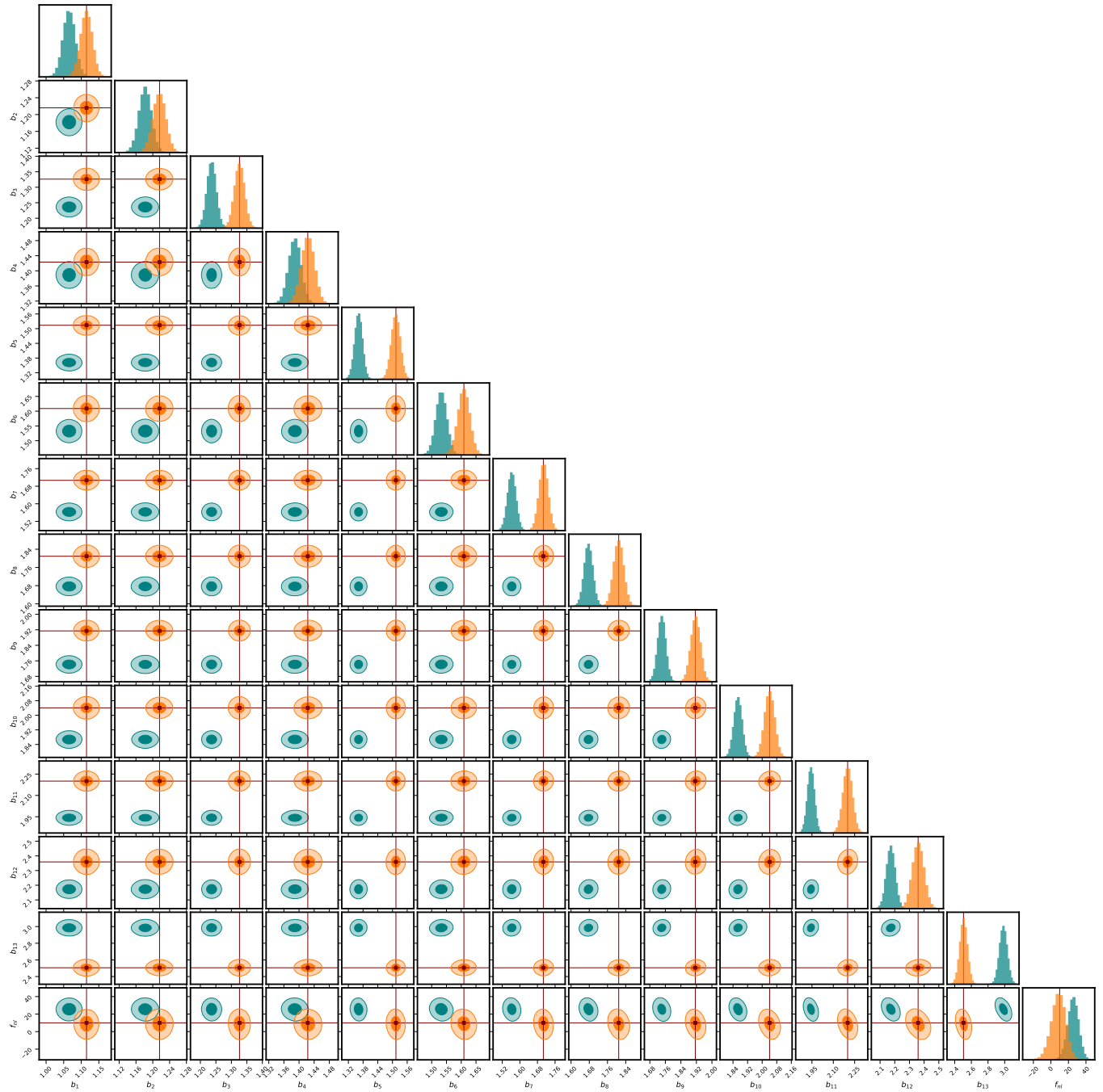


Figure 9. Same as Fig. 8 but for  $f_{NL}^{loc,true} = 10$

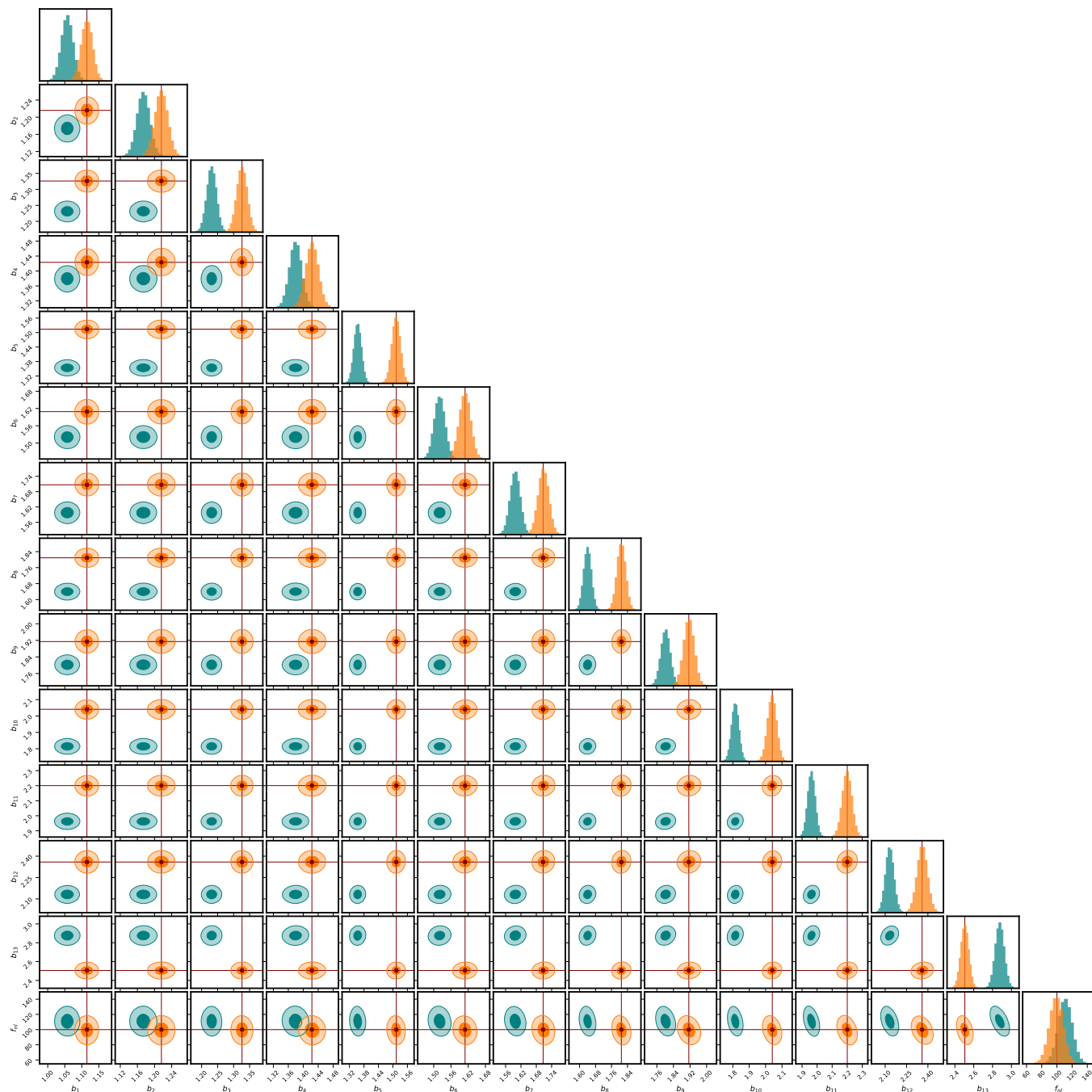


Figure 10. Same as Fig. 8 but for  $f_{NL}^{\text{loc,true}} = 100$